Journal of Computational Physics **150,** 482–501 (1999)
Article ID jcph.1999.6191, available online at http://www.idealibrary.com on IDEAL®

Implementation Aspects of 3D Lattice-BGK: Boundaries, Accuracy, and a New Fast Relaxation Method

D. Kandhai,* A. Koponen,† A. Hoekstra,* M. Kataja,† J. Timonen,† and P. M. A. Sloot*

**Department of Mathematics, Computer Science, Physics, and Astronomy, University of Amsterdam, Kruislaan 403, NL-1098 SJ Amsterdam, The Netherlands; †Department of Physics, University of Jyväskylä, P.O. Box 35, FIN-40351 Jyväskylä, Finland*
E-mail: *{kandhai, alfons, peterslo}@wins.uva.nl, †{antti.koponen, markku.kataja, jussi.timonen}@phys.jyu.fi

Received March 12, 1998; revised November 17, 1998

In many realistic fluid-dynamical simulations the specification of the boundary conditions, the error sources, and the number of time steps to reach a steady state are important practical considerations. In this paper we study these issues in the case of the lattice-BGK model. The objective is to present a comprehensive overview of some pitfalls and shortcomings of the lattice-BGK method and to introduce some new ideas useful in practical simulations. We begin with an evaluation of the widely used bounce-back boundary condition in staircase geometries by simulating flow in an inclined tube. It is shown that the bounce-back scheme is first-order accurate in space when the location of the non-slip wall is assumed to be at the boundary nodes. Moreover, for a specific inclination angle of 45 degrees, the scheme is found to be second-order accurate when the location of the non-slip velocity is fitted halfway between the last fluid nodes and the first solid nodes. The error as a function of the relaxation parameter is in that case qualitatively similar to that of flat walls. Next, a comparison of simulations of fluid flow by means of pressure boundaries and by means of body force is presented. A good agreement between these two boundary conditions has been found in the creeping-flow regime. For higher Reynolds numbers differences have been found that are probably caused by problems associated with the pressure boundaries. Furthermore, two widely used 3D models, namely D_3Q_{15} and D_3Q_{19}, are analysed. It is shown that the D_3Q_{15} model may induce artificial checkerboard invariants due to the connectivity of the lattice. Finally, a new iterative method, which significantly reduces the saturation time, is presented and validated on different benchmark problems.

Key Words: lattice-BGK model; accuracy; boundary conditions.

0021-9991/99 $30.00

I. INTRODUCTION

The lattice-Boltzmann method [1–4] is a mesoscopic approach based on the kinetic Boltzmann equation for simulating fluid flow. In this method fluid is modeled by particles moving on a regular lattice. At each time step particles propagate to neighboring lattice points and re-distribute their velocities in a local collision phase. This model has been successfully used for simulating many complex fluid-dynamical problems, such as suspension flow, multi-phase flow, and fluid flow in porous media, which are quite difficult to simulate by conventional methods [3]. Moreover, the inherent locality of the update rules makes it ideal for parallel computing [5].

During the past few years much progress has been made in the development of the lattice-Boltzmann method. Different models for simulating a wide variety of physical systems have been developed [1–3, 6–10, 12, 13], various ways of imposing boundary conditions have been proposed [14–19], and lately several schemes based on non-uniform lattices have been reported [21–23]. In this article we study some important aspects which are of practical significance. We will focus our attention on the boundary conditions, the regularly used 3D models, and the saturation time (that is, the number of time steps needed to reach a steady state) of the model.

The actual specification of the boundary conditions in lattice-Boltzmann simulations has attracted much attention. Previous studies show that the effect of the bounce-back rule, which is widely used to model a solid wall, is certainly not trivial [15–17, 24]. We study the behavior of this boundary condition for staircase boundaries. Furthermore, in many lattice-Boltzmann simulations fluid is driven by a body force [25]. This approach is well suited for periodic geometries. More sophisticated pressure- and velocity-boundaries have been proposed by several authors to model the inlets and outlets of non-periodic systems [26, 27]. We present a comparison of the body force and pressure boundaries in order to gain more insight into the accuracy of these approaches.

In 3D lattice-Boltzmann simulations the regularly used models are the D_3Q_{15} and the D_3Q_{19} model (here D denotes the dimensionality of the problem and Q is the number of bonds per lattice point) [9]. We will show that, in the D_3Q_{15} model, there can appear checkerboarding in the fluid momentum. In some cases this unphysical effect seems to be suppressed by boundaries. We will also discuss in some detail the numerical accuracy of these models.

As most numerical algorithms, the standard lattice-Boltzmann scheme also has potential shortcomings. For instance, in many cases the number of time steps needed to reach the steady state is very high. It can be argued that this is a direct consequence of the transient nature of the scheme. Here, we will present a new technique, namely the Iterative Momentum Relaxation technique (IMR), which can significantly reduce the saturation time of simulations driven by a body force.

In Section II we first review the basics of the lattice-Boltzmann method. In Section III we discuss the bounce-back boundary condition and the accuracy of the body-force method. In Section IV we study various 3D models and, especially, the checkerboard effect. Finally, in Section V, we present the IMR technique.

II. THE LATTICE-BOLTZMANN METHOD

Basically, the time evolution of the lattice-Boltzmann model consists of a propagation phase, where particles move along lattice bonds from a lattice node to one of its neighbors,

and a collision phase with a local redistribution of the particle densities subject to conservation of mass and momentum. The simplest and currently widely used lattice-Boltzmann model is the so-called lattice-BGK (Bhatnagar–Gross–Krook) model. Here the collision operator is based on a single-time relaxation to the local equilibrium distribution [2, 9].

In the literature different formulations of the lattice-BGK model can be found. The differences lie, e.g., in the connectivity of the lattice used. In two dimensions 7 or 9 links per lattice point (the D_2Q_7 and D_2Q_9 models, respectively) are frequently used, while in three dimensions 15 or 19 links per lattice point (the D_3Q_{15} and D_3Q_{19} models, respectively) are regularly used, in addition to models without rest particles (the D_3Q_{14} and D_3Q_{18} models). In this paper the D_2Q_9 model is used in the two-dimensional simulations, whereas in three dimensions the D_3Q_{15} and the D_3Q_{19} models will be considered. In the D_2Q_9 model each lattice point is connected to its eight nearest and diagonal neighbors. In the D_3Q_{19} model each lattice point is connected to its six nearest and twelve diagonal neighbors at a distance of $\sqrt{2}$, while in the D_3Q_{15} model each lattice point is connected to its six nearest and eight diagonal neighbors at a distance of $\sqrt{3}$ (see Fig. 6). Rest particles are included in all three models.

The time evolution of the lattice-BGK model is given by [9]

$$f_i(\mathbf{r}+\mathbf{c}_i, t+1) = f_i(\mathbf{r}, t) + \frac{1}{\tau}\left(f_i^{(0)}(\mathbf{r}, t) - f_i(\mathbf{r}, t)\right), \tag{1}$$

where $\mathbf{c}_i$ is the ith link (bond), $f_i(\mathbf{r}, t)$ is the density of particles moving in the $\mathbf{c}_i$ direction, τ is the BGK relaxation parameter, and $f_i^{(0)}(\mathbf{r}, t)$ is the equilibrium distribution function towards which the particle population is relaxed. The hydrodynamic fields, such as the density ρ and the velocity $\mathbf{v}$, are obtained from moments of the discrete velocity distribution $f_i(\mathbf{r}, t)$,

$$\rho(\mathbf{r}, t) = \sum_{i=0}^{N} f_i(\mathbf{r}, t) \qquad \text{and} \qquad \mathbf{v}(\mathbf{r}, t) = \frac{\sum_{i=0}^{N} f_i(\mathbf{r}, t)\mathbf{c}_i}{\rho(\mathbf{r}, t)}, \tag{2}$$

where N is the number of links per lattice point.

The equilibrium distribution function can be chosen in many ways. A common choice is [9]

$$f_i^{(0)} = t_i\rho\left(1 + \frac{1}{c_s^2}(\mathbf{c}_i\cdot\mathbf{v}) + \frac{1}{2c_s^4}(\mathbf{c}_i\cdot\mathbf{v})^2 - \frac{1}{2c_s^2}v^2\right), \tag{3}$$

where t_i is a weight factor depending on the length of the vector $\mathbf{c}_i$, and c_s is the speed of sound. For the weight factors used in the different models see Table I.

TABLE I
The Coefficients t_i in the Equilibrium Distribution Function $f_i^{(0)}$ for the Different Lattice-BGK Models [9, 29]

Model	0	I	II	III
D_2Q_9	$\frac{4}{9}$	$\frac{1}{9}$	$\frac{1}{36}$	0
D_3Q_{15}	$\frac{2}{9}$	$\frac{1}{9}$	0	$\frac{1}{72}$
D_3Q_{19}	$\frac{1}{3}$	$\frac{1}{18}$	$\frac{1}{36}$	0

Note. A 0 indicates a rest particle, I is for links pointing to the nearest neighbors, II is for the links pointing to the next-nearest neighbors, and III is for the next-next-nearest neighbors.

The lattice-Boltzmann models presented here yield the correct hydrodynamic behavior for an incompressible fluid in the limit of low Mach and Knudsen numbers [9]. The kinematic viscosity of the simulated fluid ν and the speed of sound c_s expressed in lattice units are $\nu = \frac{\tau - 1/2}{3}$ and $c_s = \sqrt{(1/3)}$ [9]. The fluid pressure $p(\mathbf{r}, t)$ is given by

$$p(\mathbf{r}, t) = c_s^2(\rho(\mathbf{r}, t) - \bar{\rho}), \tag{4}$$

where $\bar{\rho}$ is the mean density of the fluid.

III. THE BOUNDARY CONDITIONS

The numerical quality of lattice-Boltzmann simulations is determined by the following error sources:

(1) Finite-size effects due to an insufficient number of lattice points compared to the mean free path of the fluid particles. These, Knudsen-like effects, depend on both the relaxation parameter (controls the mean free path) and the lattice resolution [27].

(2) Compressibility errors. Compressibility effects are caused by the fact that in the lattice-Boltzmann method small fluctuations in the density are associated with variations in pressure. The compressibility error is small for low Mach numbers [29].

(3) Boundary effects. In principle, the truncation error of the lattice-Boltzmann method is second-order in space. However, the accuracy of the solution depends on the boundary conditions and is found to be only first-order in many cases [15–17, 19, 27]. Understanding the effect of the boundary conditions is very important since they are crucial in many fluid-dynamical simulations. In this section we will study boundary conditions for two common cases, namely the bounce-back boundary condition at a solid wall and the body force, which is often used as a substitute to pressure boundaries.

A. *The Bounce-Back Boundary Condition*

The bounce-back boundary rule is the simplest way to impose solid walls in lattice-Boltzmann simulations. Here, particles that meet a wall point are simply bounced back with a reversed velocity. It is obvious that this rule leads to a non-slip boundary located *somewhere between* the wall nodes and the adjacent fluid nodes (in the literature this effect is known as the shift of the boundary). More sophisticated boundaries, which model a non-slip boundary exactly at the wall node (the so-called second-order boundaries), have been proposed by several authors [15–19, 27, 20]. Unfortunately most of them are restricted to regular geometries (like flat walls and octagonal objects) [15–17]. For practical simulations the bounce-back boundary is very attractive because it is a simple and computationally efficient method for imposing non-slip walls with irregular geometries.

Most previous studies of bounce-back have considered only flat walls, although a few more detailed studies have also been published. Recently, an evaluation of the bounce-back method has been reported where the solutions obtained with the bounce-back rule were compared with those obtained with the finite-difference method for flow around octagonal and circular objects [30]. In this analysis the location of the non-slip boundary was thus taken to be at the wall node itself and the error in the solution was first-order convergent in space. Here we will study the behavior of the bounce-back boundary for a similar staggered geometry. Beside the standard analysis, where the location of the non-slip boundary is

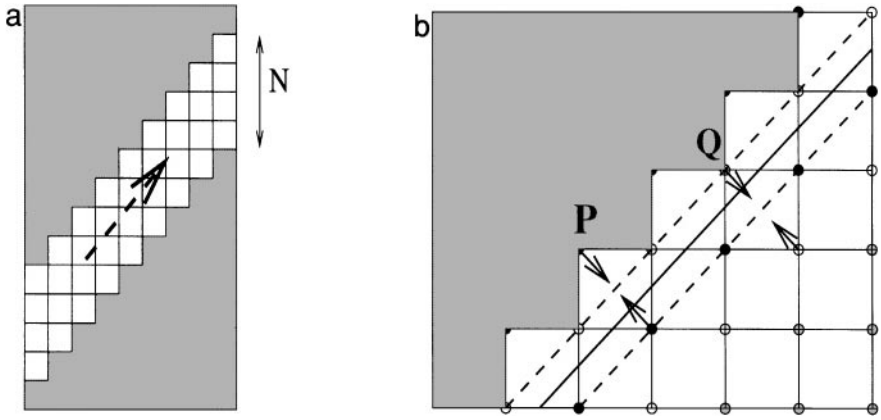

FIG. 1. The inclined tube flow experiment for an inclination angle of 45 degrees. On the left the computational grid is shown and on the right the location of the wall.

assumed to be at the wall node, our benchmark problem enables us to study the shift of the boundary for a specific staircase geometry, as will be shown in the following.

We chose the simple Poiseulle flow in a tilted channel as our benchmark problem. In this case the analytical solution for the velocity profile is known, and the effect of the bounce-back rule in a staircase boundary can be investigated by simulating fluid flow through an inclined tube (see Fig. 1a). The analytical solution for this problem (in lattice units) is given by

$$u_j = u_0 * \left(1 - \frac{j^2}{l^2}\right), \tag{5}$$

where u_j is the component of the velocity vector along the flow direction at a distance j from the center of the tube, l is the radius of the tube, and u_0 is the maximum velocity [11]. The absolute and relative errors at location j, ϵ_j^{abs}, and ϵ_j^{rel}, respectively, are defined as

$$\epsilon_j^{abs} = |u_j - \bar{u}_j|, \qquad \epsilon_j^{rel} = \left|\frac{u_j - \bar{u}_j}{u_j}\right|, \tag{6}$$

where $\bar{u}_j$ is the simulated velocity at location j.

Periodic boundaries were imposed at the inlet and outlet of the tube, and a constant body force was used to drive the flow (i.e., a fixed amount of momentum $\mathbf{q}$ was added at every time step on each lattice point). The body force was directed along the flow direction, and periodic boundaries were implemented by taking into account the translation of the inlet and outlet in the vertical direction. The walls were modeled by the bounce-back boundary rule.

The mean relative error as a function of lattice spacing is shown in Fig. 2 for the standard bounce-back analysis. In this figure we have included the results for the inclination angle $\alpha = 0$, 15, 30, and 45 degrees. A first-order convergence of the mean relative error is found in all cases (a fit to the data points gives a slope of -0.9). Furthermore, the error for the staircase geometries is on the average 50% higher than for the flat walls. The relative error close to the boundary nodes (very small velocities) is significantly higher than along the center of the tube. For staircase geometries, there is no clear dependence of the relative

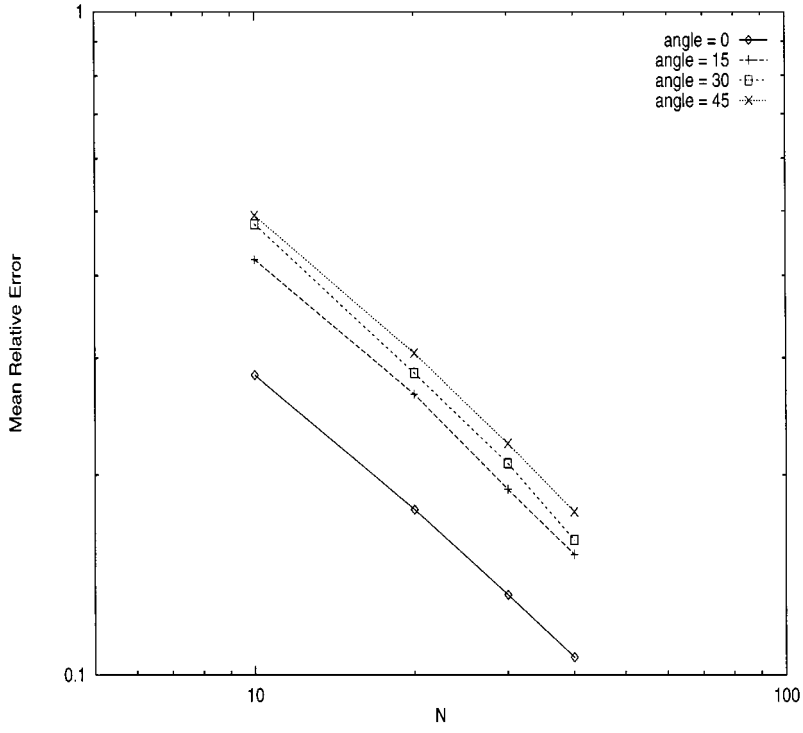

FIG. 2. The mean-relative error in the inclined-tube flow simulations (angles 0, 15, 30, and 45 degrees) for the standard bounce-back analysis. Tube diameter is 10, 20, 30, and 40 lattice-points, $v_0 = 0.01$, and $\tau = 1.0$. The length of the tube is 40 lattice-points.

error on the inclination angle, because the differences between the relative error for $\alpha = 15$, 30, and 45 degrees are smaller than the fluctuations in the error along the tube. Moreover our results are of the same order as those of Gallivan *et al.* [30] for flow around octagonal cylinders when similar error metrics are used (data not shown).

As discussed previously, the accuracy of the simulation is determined by the location of the non-slip wall. For tube flow in flat geometries, it has been shown both numerically and analytically, that when the non-slip boundary is assumed to be in the middle of the first wall and the last fluid node, the error is second-order convergent [24]. In this case the analytic expression for the absolute error caused by the bounce-back boundary condition is given by [24]

$$u_j - \bar{u}_j = -\frac{u_0(4\tau(4\tau - 5) + 3)}{3(2l - 1)^2}. \tag{7}$$

Notice that, according to Eq. (7), this "half-way shifted" wall is quite an accurate boundary condition for practical values of the relaxation parameter [24]. Furthermore, the error, $u_j - \bar{u}_j = 0$, when the relaxation parameter is $\tau = 1.07$. We have found very good agreement between our simulations and Eq. (7) (data now shown).

As a final case, we have studied whether such a shift of the boundary can be seen in staircase geometries, by determining the error behavior as a function of the lattice dimensions and the relaxation parameter. We have restricted our analysis to an inclination angle of 45 degrees. The "half-way shifted" location of the wall is expected to differ somewhat

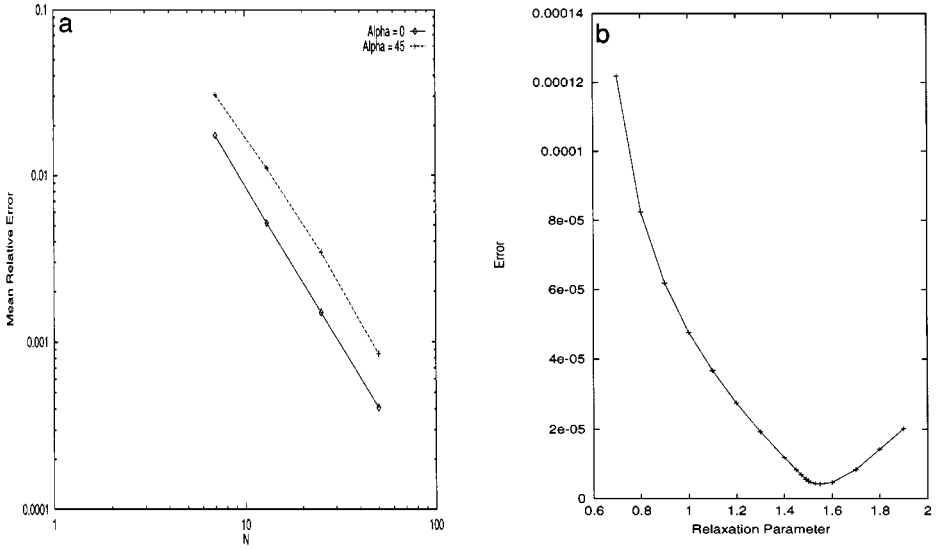

FIG. 3. (a) The mean-relative error on lattices with $N = 7$, 13, 25, and 50 lattice points. Square (slope of the line is -2.0) and stars (slope is -1.9) are the half-way shifted results for flat and 45 degrees inclined tube, respectively, $v_0 \approx 0.01$, and $\tau = 1.0$. The length of the tube is 40 lattice-points. (b) The mean-relative error as a function of τ for $N = 25$ and $v_0 = 0.1$. The length of the tube is 40 lattice-points.

from that of a flat tube. In Fig. 1b we show the "half-way shifted" location of the wall. The staircase geometry is staggered between two straight lines (lines through the type-P and type-Q points in Fig. 1b). Therefore, the "half-way shifted" boundary is also staggered between two straight lines (dashed lines in Fig. 1b). The location of the boundary is taken as the average of these two lines (see the thick solid line in Fig. 1b).

The mean relative error as a function of lattice spacing is shown in Fig. 3a. In this figure we have included two curves, namely the results for the flat tube and the inclined tube experiment, where for both cases the wall is placed at the "half-way shifted" location. For both cases the error is second-order convergent (a fit to the data points gives an approximate convergence of -1.9). Furthermore, we clearly see that the mean relative error for the flat tube is somewhat smaller than that for the inclined tube. In Fig. 3b the error as a function of the relaxation parameter is shown. A qualitatively similar error behavior for the inclined- and flat-tube flow (Eq. (7)) is found. For an increasing relaxation parameter, the error first decreases and subsequently increases after some optimal value of the relaxation parameter. Here we observe that, for practical values of the relaxation parameter, the "half-way shifted" boundary is quite accurate. The optimal relaxation parameter in this case is approximately 1.55.

We have seen that the error due to staircased structure is on the average 50% higher than for flat geometries. For a specific case ($\alpha = 45$ degrees), we have verified that the bounce-back boundary rule tends to generate an imaginary boundary, which is located between the last fluid node and the solid wall. For the general case it is expected that the exact location of the boundary will depend on the relaxation parameter and the geometry of the problem. We think that it is very difficult to predict the location of the non-slip wall for arbitrary geometries. For geometries with finite curvatures, e.g., for spherical particles, we have found that the difference between the hydrodynamic radius and the actual radius is

quite small when the relaxation parameter is taken to be $0.7 \leq \tau \leq 1.3$, and the particle radius is expressed in the units of half lattice spacing (cf. Section 4). Also, we have recently performed a detailed comparison between the lattice-Boltzmann method, the Finite Element method, and experimental data for fluid flow in a complex 3D chemical mixing reactor [32]. The geometry of the reactor consisted of a number of solid tubes in different orientations and locations and was such that it promoted mixing of fluid flowing through it. The results of the lattice-Boltzmann simulations were quite satisfactory even on moderate lattices. Supported by these results, we thus conclude that in irregular geometries the bounce-back boundary is certainly very useful despite its simplicity. In some applications, however, sufficient accuracy may only be obtained on large lattices. In such cases, the accuracy can be increased by locally refining the grid in the vicinity of solid walls.

B. *Comparison between Body Force and Pressure Boundaries*

Successful numerical simulation of practical fluid-flow problems requires that the velocity and pressure boundary conditions have been set in a consistent way. However, general velocity and pressure boundaries are still under further development for the lattice-Boltzmann method [3, 10, 12, 13, 15–17, 19, 27, 34–36]. So far practical simulations have usually included first-order velocity boundaries [29, 37], and a body force [3, 25, 31, 39] has often been used instead of pressure boundaries in problems with a periodic geometry.

Consider, e.g., fluid flow through an infinite vertical array of cylinders, where pressure is kept constant in vertical planes in front and beyond the cylinders (see Fig. 4). Here, the use of body force instead of pressure boundaries is based on the assumption that the effect of the external pressure force $(p_1 - p_2)L_y\mathbf{e}_x \equiv Q\mathbf{e}_x$ is approximately constant everywhere in the system. Provided that this indeed is the case, and that the densities at the inlet and outlet surfaces are kept constant, pressure boundaries can be replaced with a global body force $Q\mathbf{e}_x$ that gives rise to an acceleration $g\mathbf{e}_x$ of the fluid. Pressure fields are then obtained from the effective pressure p_{eff}, which is defined as

$$p_{eff} = c_s^2 \Delta\rho - \bar{\rho} g x, \tag{8}$$

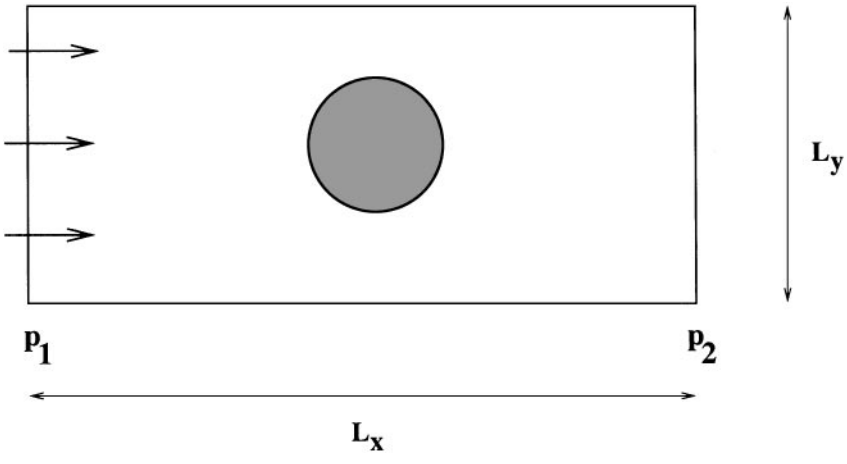

FIG. 4. One unit shell in a vertically infinite array of cylinders. L_x and L_y are the length and the width of the unit shell, and p_1 and p_2 are the fluid pressures at the inlet and outlet, respectively.

where x is the distance measured from the inlet of the system. Notice that, for a simple tube flow, the body force approach is an accurate substitute to pressure boundaries in that, i.e., the velocity and pressure fields given by the two methods are identical.

In order to check the validity of the body-force approach, we simulated the system shown in Fig. 4 with both the body force and the pressure boundaries. The simulation lattice was $L_x \times L_y = 300 \times 100$ lattice points, the cylinder radius a_0 was 5.5 lattice points, the center of the cylinder was located 100 lattice points from the inlet, and periodic boundaries were used in the y direction. The cylinder Reynolds number, $\mathrm{Re} = 2a_0U/\nu$, was varied between 0 and 6 by adjusting the LBGK relaxation parameter τ between 0.6 and 2.0.

In the body-force simulations periodic boundaries were used also in the x direction. Density, and thus effective pressure, were kept constant at the inlet and outlet. The fluid momentum was also kept constant to prevent the cylinders from seeing their periodic images in the x direction. This was done as follows: after the propagation step the average fluid densities ρ_{in} and ρ_{out}, and the average velocities $\mathbf{v}_{in} = \mathbf{P}_{in}/\rho_{in}$ and $\mathbf{v}_{out} = \mathbf{P}_{out}/\rho_{out}$, were first calculated at the inlet and outlet, respectively. (Here $\mathbf{P}_{in}$ and $\mathbf{P}_{out}$ are the corresponding total fluid momenta.) Then the particle densities f_i at the inlet and outlet were set to $f_{i,in} = f_i^{(0)}(\rho_{in}, \mathbf{v}_{in})$ and $f_{i,out} = f_i^{(0)}(\rho_{out}, \mathbf{v}_{out})$, respectively.

Pressure boundaries were implemented by the method described in Ref. [27]. Because in both cases velocity and pressure can develop freely, and the channel is big compared with the size of the cylinder (some preliminary finite-size simulations were performed as a verification), the conditions close to the cylinders are very similar in both simulations.

Notice that, when the system is fully saturated, the drag force acting on the obstacle completely cancels the effect of pressure or body force. So, if the pressure boundary of Ref. [27] is accurate, the two different methods should give equal drag forces, although the simulated velocity and pressure fields may be different.

In Table II we show for different Reynolds numbers the relative difference in the velocity, pressure, and the drag forces acting on the particle, between the pressure boundary and the body force simulations. The difference is calculated in a box of 60×50 lattice spacings around the obstacle. The relative error in the velocity, ϵ_v is defined as $\epsilon_v = (v_p - v_b)/v_p$, where v_p and v_b are the velocities of the pressure boundary and body force simulations, respectively, and the relative error in the pressure is defined as

$$\epsilon_p = (\delta p - \delta p_{eff})/\delta p_{12}, \tag{9}$$

TABLE II

The Mean and Maximum Relative Error in the Velocity, ϵ_v, Pressure, ϵ_p, and the Drag Forces Acting on the Particle, ϵ_{drag}, between Pressure Boundary and Body Force Simulations for Different Reynolds Numbers

Re	0	0.05	0.4	2	3	6
Mean ϵ_v	0.33	0.34	0.33	0.34	1.36	2.2
Max ϵ_v	0.81	0.96	0.79	0.86	2.35	62
Mean ϵ_p	0.24	0.24	0.27	0.46	1.9	3.94
Max ϵ_p	0.97	0.90	0.92	1.92	6.2	14.1
ϵ_{drag}	$1.2 \cdot 10^{-8}$	$8 \cdot 10^{-4}$	$7.3 \cdot 10^{-3}$	$7.7 \cdot 10^{-2}$	1.1	2.6

Note. The numbers are expressed in percentages.

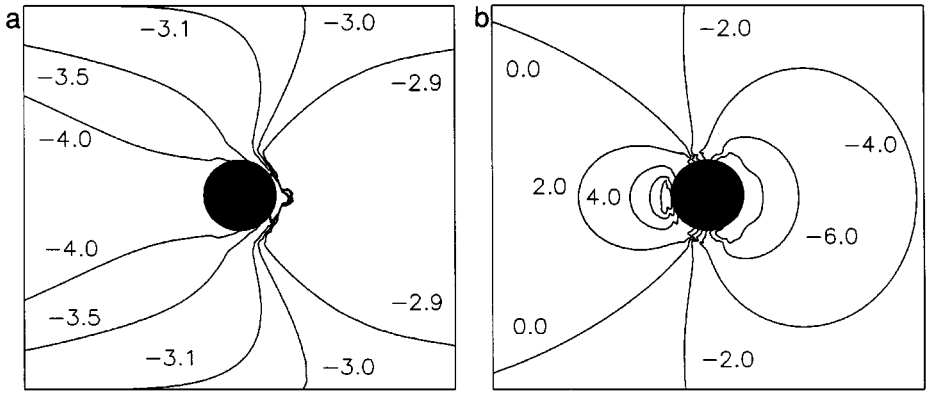

FIG. 5. Comparison of relative error of velocity (a) and pressure (b) for body force and pressure boundaries. The numbers are expressed in 1/1000 in both cases. The flow is from left to right.

where $\delta p = p_{in} - p$ and $\delta p_{eff} = p_{eff,in} - p_{eff}$ are the pressure differences between the inlet and a point (x, y) for the pressure boundary and body force simulations, respectively. We chose $\delta p_{12} = p_1 - p_2$ as the reference scale instead of δp, because on many lattice points δp was very close to zero. We clearly see that for $\mathrm{Re} \leq 2$ the mean relative difference in pressure and velocity is less than 1%. For higher Reynolds numbers bigger differences are found. These are probably caused by problems related to the pressure boundary conditions, because the drag in the pressure boundary simulations was not in good agreement with the expected value, in contrast with the results of the body-force simulations.

In Fig. 5a we show the contour plot of the relative error ϵ_v for $\mathrm{Re} = 0.4$. The pressure boundary simulations regularly gave a little smaller velocities, the average error being $|\epsilon_v|_{ave} = 0.33\%$. The biggest differences in the velocities, namely 0.79% and -0.74%, were found at the up-stream and down-stream stagnation points, respectively. The contour plot of ϵ_p is shown in Fig. 5b. Its average value was $|\epsilon_p|_{ave} = 0.27\%$. The maximum and minimum values for ϵ_p, namely 0.87% and -0.92%, are once again found at the stagnation points.

In addition to this benchmark, we studied a more complicated case, namely fluid flow in a disordered porous medium composed of nonoverlapping cylinders. The radii of the cylinders were $a_0 = 5.5$ lattice spacings, the porosity of the medium was 0.8, and $\tau = 1.0$. The lattice dimensions were $L_x \times L_y = 500 \times 100$, and the porous medium was placed at a distance of 200 lattice spacings from the inlet and outlet. The obstacle Reynolds numbers were on average 0.003. The difference in the total drag given by the pressure boundary and body-force simulations was quite high, namely 4%. The average relative errors $|\epsilon_v|_{ave}$ and $|\epsilon_p|_{ave}$ in the velocity and pressure fields were 4.2 and 2.2%, respectively, and the maximum errors of $|\epsilon_v|$ and $|\epsilon_p|$ were 28 and 4.3%. Thus, although the error in total drag was quite big, the overall results were still quite satisfactory. In this paper we have used the drag force acting on the particle as a reference. More detailed comparison of the complete velocity and pressure profiles for body-force driven simulations with results of traditional methods and experimental data of different problems for a wide range of Reynolds numbers can be found in Refs. [32, 33].

We can conclude that, for small Reynolds numbers and simple geometries, the body-force approach is quite an accurate substitute to pressure boundaries. However, for high

Reynolds-number flows, where nonlinear effects are dominant, and for more complicated geometries, more sophisticated pressure boundaries may still be needed.

IV. CHECKERBOARD EFFECT IN THE D_3Q_{14} AND D_3Q_{15} MODELS

The lattice-Boltzmann method was originally developed from the lattice-gas automata. The first lattice used in 3D simulations was the D_3Q_{19} lattice [1], which is a 3D projection of the 4D FCHC lattice [3] used for 3D lattice-gas simulations (see Fig. 6a).

It was later realized that the relative freedom in choosing the lattice-Boltzmann equilibrium distribution function also gave some freedom in choosing the structure of the simulation lattice. As a result, the D_3Q_{15} model (see Fig. 6b) was developed [9]. The D_3Q_{14} and D_3Q_{18} models are obtained from the D_3Q_{15} and D_3Q_{19} models, respectively, by excluding the rest particles. However, the presence of rest particles is often desirable for improving the accuracy of the model [40]. Also, for a small relaxation time τ, the rest particles may be needed to stabilize the system [42]. Therefore, the D_3Q_{15} and D_3Q_{19} models are most often used in practical simulations.

The computational and the memory requirements of the lattice-Boltzmann model scale linearly with the number of fluid particles. The D_3Q_{14} and D_3Q_{15} models are thus somewhat more efficient than the D_3Q_{18} and D_3Q_{19} models. However, in the D_3Q_{14} and D_3Q_{15} models, checkerboard behavior in the fluid momentum can occur, i.e., fluid momentum may form unphysical regular patterns. We will demonstrate this below in the case of saturation of a random velocity field and in the case of fluid flow around a spherical obstacle.

Let us mark the lattice points (i, j, k) by black colour if $i + j + k$ is odd, and by white colour otherwise, thus forming a checkerboard pattern shown in Fig. 6 for the D_3Q_{19} and D_3Q_{15} models. To each lattice-Boltzmann fluid particle, we also assign the colour of the lattice point at which they reside in the beginning of the simulation. If there are no obstacles in the system, it is easy to see that, in the D_3Q_{14} model, the black and white particle populations are completely independent of each other: the colour of the lattice point at which a given fluid particle resides changes at every time step (see Fig. 6b). As a

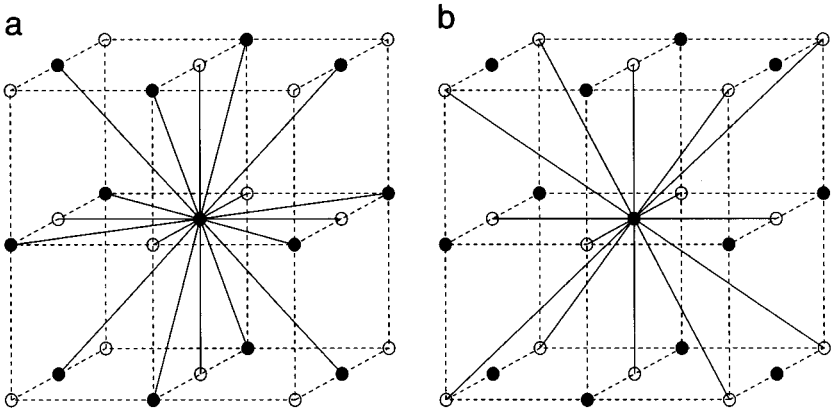

FIG. 6. Lattice structures of D_3Q_{19} and D_3Q_{15} lattice-BGK models. The checkerboard coloring is included in the figures. On the left the D_3Q_{19} model is shown and on the right the D_3Q_{15} model.

consequence of this checkerboard effect, the total mass and momentum of the black and white particle populations are spurious invariants, i.e., unphysical conserved quantities in the D_3Q_{14} model. Similar spurious invariants are also found in the HPP lattice-gas model [28]. These invariants can create unphysical hydrodynamic modes in the simulated system, and for this reason they should be eliminated from the model [3]. Notice that, in the D_3Q_{18} model, the black and white populations mix immediately with each other. Consequently, there is no checkerboard effect in this model.

In the D_3Q_{15} model the black and white populations are not entirely independent as they are coupled through the rest particles. However, checkerboard effects may also here lead to unphysical behavior. If the lattice is initialized with equilibrium distribution such that, e.g., the velocity is set to $\mathbf{u}_b$ at black lattice points and to $\mathbf{u}_w$ at the white lattice points, while $|\mathbf{u}_b|$ is equal to $|\mathbf{u}_w|$, it is easy to see that the total momenta of the black and white populations will be conserved quantities.

We studied the checkerboard effect by following the relaxation of a perturbed velocity field with a constant initial density and with periodic boundaries imposed in all directions. We used two different lattices. In the first case the lattice dimensions were $10 \times 10 \times 10$ lattice points. When a steady state was reached in the D_3Q_{19} model, all components of the particle momenta were found to oscillate at each lattice point between two values (see Fig. 7a). Such oscillations are caused by the so-called staggered invariants [10]. They can be removed with proper initial conditions, and their effect can also be filtered out by averaging the momenta over two steps. After time averaging the momentum field was uniform, as expected [10]. In the D_3Q_{15} model, the fluid remained partially unmixed in the steady state. After time averaging, two different values for the particle momenta were found in the lattice (see Fig. 7b), and each component of momentum was constant along lines parallel to the corresponding direction. The x component, e.g., was constant on lines parallel to the x axis, and its distribution in the yz plane formed a checkerboard pattern. The relative difference between the two values of the momentum varied in the simulations, being typically 0.5–3%.

Similar simulations were also performed on a $9 \times 9 \times 9$ lattice. In this case the two populations had additional mixing on the boundaries of the lattice, as the colouring rule

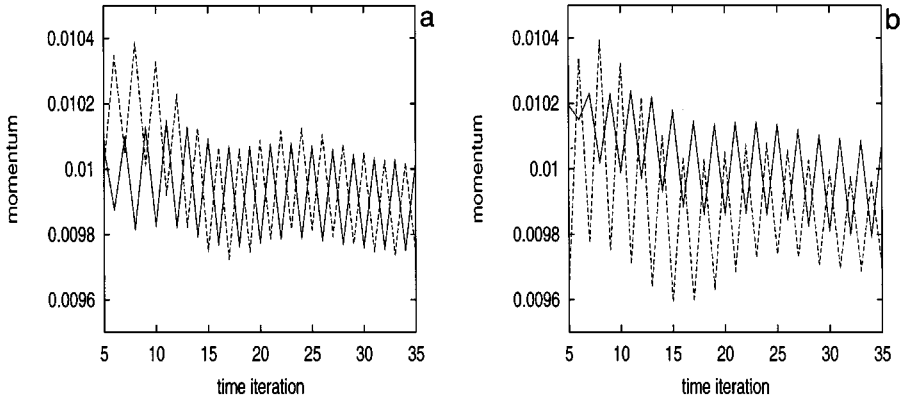

FIG. 7. Relaxation of the x components of the momenta of two next-nearest neighbors in the xy plane on a lattice of dimension $10 \times 10 \times 10$. On the left the right we show the time evolution of the D_3Q_{19} and D_3Q_{15} models, respectively. The initial perturbed velocity field is the same in both models.

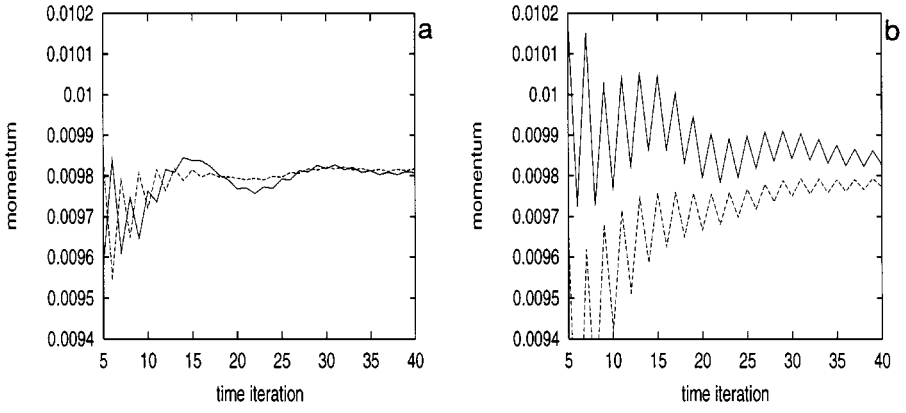

FIG. 8. Relaxation of the x components of the momenta of two next-nearest neighbors in the xy plane on a $9 \times 9 \times 9$ lattice. On the left and right we show the time evolution of the D_3Q_{19} and D_3Q_{15} models, respectively.

was not continuous due to the length of the lattice being an odd number. As a result, the steady-state momentum field was uniform for both models even without time averaging, i.e., both the staggered invariants and the checkerboard effect were eliminated in the end. However, the weak coupling between the black and white populations in the D_3Q_{15} model was still apparent in the time evolution of the relaxation process. This can be seen in Fig. 8, where relaxation of the momenta of two next-nearest neighbors is shown in one direction. In the D_3Q_{15} model the relaxation process is significantly slower, and there are long-lasting oscillations in the local values of the momentum in this case.

We also studied the checkerboard effect in the presence of solid walls. The first test case was fluid flow in a rectangular duct. The duct dimensions were 30×30 lattice points, the relaxation parameter was $\tau = 1.0$, and bounce-back at the nodes was used on the solid walls. Periodic boundaries were used in the direction of flow driven by a body force. In this case no checkerboard effect were seen, and the average relative difference $|\Delta_v| = |(v_{Q19} - v_{Q15})/v_{Q19}|$ between the velocity fields given by the D_3Q_{19} and D_3Q_{15} models was only 0.34%. (A detailed duct-flow comparison between the D_3Q_{18} and D_3Q_{15} models has previously been reported in Ref. [27], where the D_3Q_{18} model was found to be more accurate in general, while the results given by the D_3Q_{15} model were also found to be satisfactory.)

The second test case was fluid flow around a sphere. The radius of the sphere was $a_0 = 5.5$ lattice points. In the first simulation, the lattice consisted of $30 \times 30 \times 30$ lattice points, and the relaxation parameter was $\tau = 1.0$. Bounce-back condition was used on the solid walls, and periodic boundaries were imposed in all directions. Flow was driven by a body force. In this case, the checkerboard effect did not lead to momentum oscillations, but appeared instead as unphysical patterns in the velocity and pressure fields. We have observed that the velocity field of the D_3Q_{15} model includes horizontal patterns which are not found in the D_3Q_{19} model. This kind of pattern is clearly seen in the values of Δv shown in Fig. 9a. Similar patterns were also seen in the values of Δp (in this comparison Δp was calculated from Eq. (8)). In Fig. 9b, the velocity profile at the inlet boundary is shown for the two models. It is evident that the D_3Q_{19} model generates a very smooth profile, whereas the D_3Q_{15} model generates a profile staggered between two smooth curves. The average

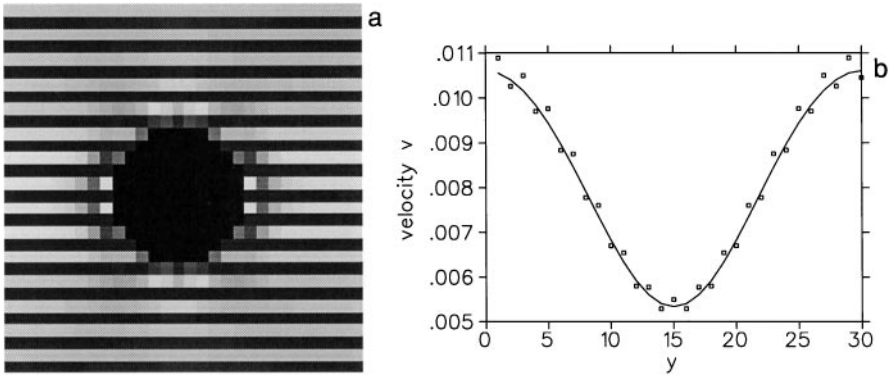

FIG. 9. The results for fluid flow around a sphere. The velocity field in a plane which bisects the sphere is analyzed. Fluid is flowing from left to right, and periodic boundaries are used in both directions. (a) The relative difference Δv between the velocity fields obtained by the D_3Q_{19} and D_3Q_{15} models. The colours run from gray to white with the scale $-3.0\% \leq \Delta v \leq 3.0\%$. (b) The velocity profile at the inlet for both models. The solid line and open boxes show the results for the D_3Q_{19} and D_3Q_{15} models, respectively.

values of $|\Delta v|_{ave}$ and $|\Delta p|_{ave}$ were 2.5 and 3.9%, respectively. The difference between the total momenta of the fluids was in steady state only 0.62%. For this reason, e.g., the hydrodynamic radii a of the sphere (a detailed description of the determination of a is found in Ref. [10]) given by these models were very close to each other: the D_3Q_{15} and D_3Q_{19} models gave $a = 5.50$ and $a = 5.52$, respectively. We performed similar simulations with bounce back on the links, and on a lattice of $31 \times 31 \times 31$ lattice points. Similar patterns were seen also in these two cases.

We thus conclude that, in the D_3Q_{15} model, there is a checkerboard effect which may appear in the hydrodynamic fields. In some cases the boundaries can suppress this unphysical effect. Furthermore, it does not have significant effect on global values such as the average fluid momentum. Therefore, in spite of its shortcomings, the D_3Q_{15} model appears a viable alternative for steady-state hydrodynamics.

As Fig. 8b shows, in dynamical systems (e.g., in fluid-particle suspensions or in turbulence simulations) the checkerboard effect may slow down the relaxation of momentum and can, in principle, produce unphysical effects in the dynamics of the system. Notice, however, that the solid boundaries increase mixing also in the D_3Q_{15} model in the case when bounce back on the links is used at the boundaries.

V. THE ITERATIVE MOMENTUM RELAXATION (IMR) TECHNIQUE

In lattice-Boltzmann simulations, flow is often driven by a body force which is kept constant during the simulation. Iteration is started with some initial velocity field. A steady-state solution is finally reached when the total body force $\mathbf{Q}$ acting on the fluid is completely cancelled by the viscous friction force $\mathbf{T}$ due to the walls and obstacles.

Fluid flow in random porous medium has been one important application of the lattice-Boltzmann method [25, 39, 41]. For such media, simple dimensional analysis suggests that, for a constant body force, the saturation time t_{sat} needed to reach the steady state is of the

form [18]

$$t_{sat} \propto R_{pore}^2/\nu, \tag{10}$$

where R_{pore} is the characteristic length of the void pores in the system, and ν is the viscosity of the fluid. For systems with high porosity ϕ, saturation times can therefore be very long. In some cases, tens of thousands of time steps may be needed. It is thus evident that a constant body force may be computationally inefficient, especially when one is only interested in the steady-state solution. In standard computational fluid dynamics this problem can be overcome by solving the time independent flow rather than the complete Navier–Stokes equation.

In time-dependent flows, accurate initial conditions are needed [15], whereas in time-independent flows properly chosen initial conditions may be used to speed up the saturation. Such conditions may not be easily found. However, if essential dimensionless numbers, like the Reynolds number, are kept constant, simulations may first be carried out either on a smaller lattice or for a higher viscosity. In both cases the simulation time will be smaller than in the original system. Due to discretization errors and finite size effects, the obtained velocity and pressure fields may be quite inaccurate, but they can be used as good initial guesses for the final simulation.

We will show that the saturation time can also be reduced by using an Iterative Momentum Relaxation (IMR) technique, where the applied body force is adjusted during the iteration depending on the change of fluid momentum at the iteration step considered.

In the beginning of an IMR simulation a flow is first initialized. After every t_{step} time steps, the following iterative procedure (where k denotes the iteration counter of the IMR-loop) is repeated:

(1) Calculate the momentum change $(\Delta P)_k$ of the fluid phase in the direction of the body force during the next time step.

(2) Calculate the average momentum loss $T_k = Q_k - (\Delta P)_k$ (Q_k is the total body force at the iteration step k) of the fluid due to the viscous forces during this time step.

(3) Choose a new body force as $Q_{k+1} = T_k$.

The new body force Q_{k+1} is let to accelerate the fluid during t_{step} time steps before proceeding from step (1). The simulation is carried out until the body force Q reaches an acceptable degree of convergence.

To validate the IMR technique we have applied it to three benchmark problems, namely flow around a sphere, the permeability of a 3D random fibre network (see Ref. [25]), and fluid flow in an SMRX static mixer reactor (see Ref. [32] for details). We have included the last benchmark, as it is one of the very few cases of fluid flow in complex geometries with well documented results from traditional numerical methods and experimental data. In all these test cases we have used $t_{step} = 50$. Tests with some other values of t_{step} did not show significant improvements in the benefit gained by the IMR technique.

In our first benchmark the sphere radius was $a_0 = 5.5$ lattice points and the lattice dimensions were $100 \times 100 \times 100$ lattice spacings. We performed simulations at two Reynolds numbers, namely $\mathrm{Re} = 0$ (Stokes flow) and $\mathrm{Re} = 1$. In both cases the IMR method was extremely efficient. One percent accuracy in the velocity and pressure fields was already obtained after 5000 time steps, whereas the constant body-force method would have required 180,000 times steps (data not shown).

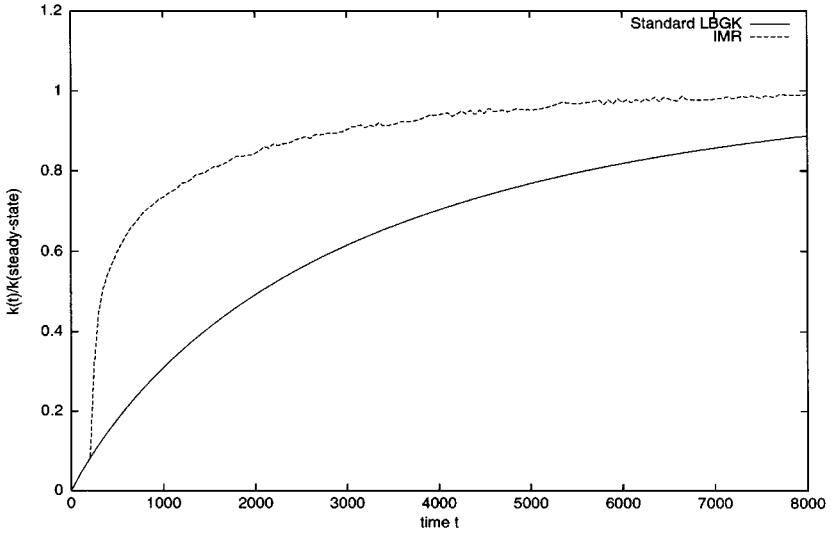

FIG. 10. The time evolution of the web permeability $k(t)/k$(steady-state) when a constant body force (solid line) or the IMR method (dashed line) is used. Permeability $k(t)$ has been computed using the body force and total fluid momentum at time step t.

In our second test case we computed the permeability k (a measure for the fluid conductivity through a porous material) of a random fiber web. The permeability can be computed from the expression $k = (\phi P \nu \rho)/(mq)$ where P is the total fluid momentum in the direction of the body force, m is the total mass of the fluid, ρ is the fluid density, and q is the body-force density in the fluid phase. In Fig. 10 we show the time evolution of the fluid momentum in a $400 \times 400 \times 60$ lattice with a porosity of $\phi = 0.94$, when a constant body force (solid line) or the IMR method (dashed line) is used. It is evident that with the IMR method an accuracy of 1% in the permeability (and thus also in the body force Q) is reached in 7000 time steps, while the constant body-force method requires more than 18,000 time steps for reaching the same level of accuracy.

Our last test case was fluid flow in a static mixer reactor (cf. Section 2 and Fig. 11). Here we have used as reference data the steady state solution of lattice-BGK simulations with a constant body-force. For an element discretization of $56 \times 56 \times 56$ lattice points, 1200 time steps were required to reach a stationary state when $\tau = 1$. In Ref. [32] we have shown in detail that these results were in good agreement with Finite Element calculations and experimental data. With the IMR technique 1% accuracy in the velocity and the pressure fields compared to our reference data, was already reached in 550 time steps, whereas the constant body-force method required 1000 time steps to reach a similar accuracy. In Fig. 12 we show the relative difference (in %) of the mean velocity, between the results of the IMR technique and our reference data. The mean velocity is computed at different cross-sections along the reactor after 500, 550, and 600 timesteps. The difference is clearly less than 1%. Similar results were also found for the other Reynolds numbers (by using a nonzero initial velocity field in the IMR technique) provided that the flow is laminar.

We conclude that at least in problems involving laminar flow, the IMR method can be very efficient in decreasing the number of time steps needed to reach the steady state. The benefit seems to depend on the complexity of the flow geometry.

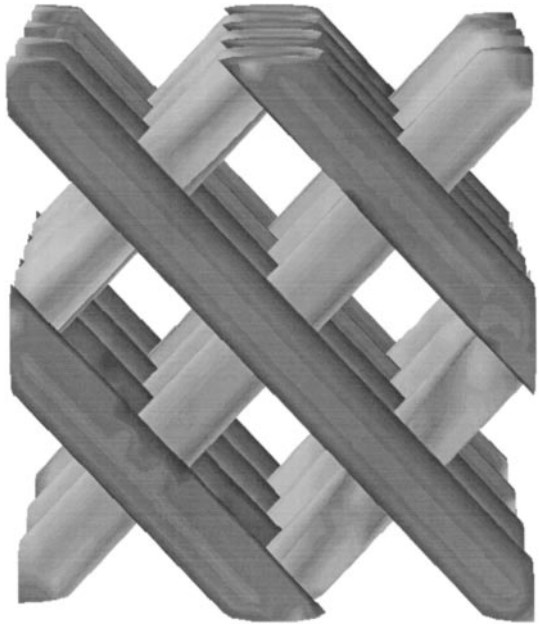

FIG. 11. The SMRX static mixer element. The reactor consists of an SMRX element placed in a rectangular duct. The inlet and outlet sections are of the same size as the element itself. The flow is from left to right.

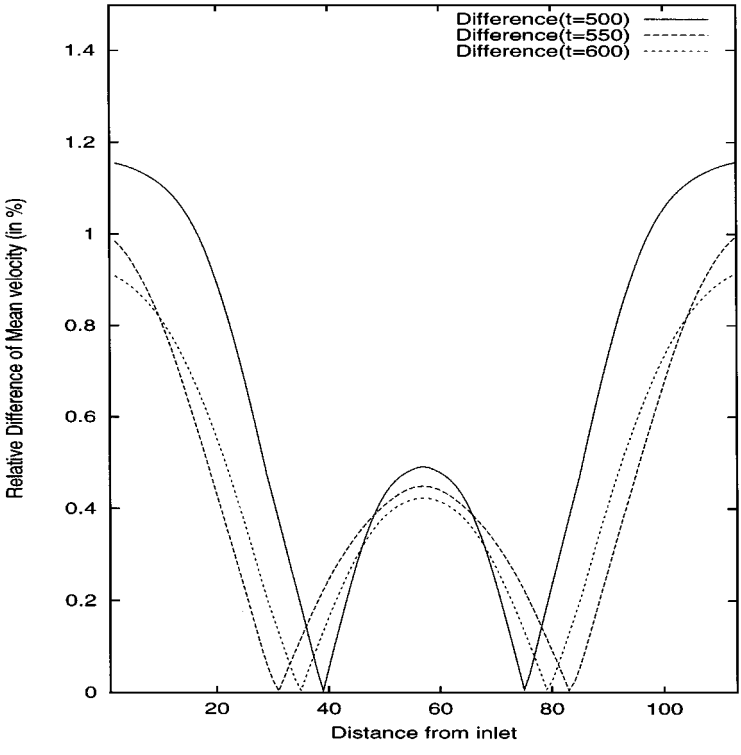

FIG. 12. The relative difference (in %) of the mean velocity between the IMR technique and the steady state solution obtained by the constant body-force approach (1200 timesteps were required). The mean velocity is computed at different cross-sections along the reactor. The relative differences at 500, 550, and 600 timesteps are shown.

VI. CONCLUSIONS

In this paper we have addressed various issues related to the lattice-BGK method which are important from a practical point of view. We first discussed the effect of the bounce-back boundary condition (which is widely used to model solid walls) for regular staircase boundaries. It was found that the error for staircased geometries is on the average 50% higher compared to that for flat walls. For a special case the bounce-back scheme was shown to be second-order convergent when the non-slip boundary was taken in the middle of the solid and adjacent fluid nodes. The quality of the method was determined by the compatibility of the shifted walls (the so-called hydrodynamic geometry) and the real geometry.

In addition, we also considered boundaries which are responsible for driving a flow between the inlet and outlet of the system. In this context we compared the well-known body-force approach with pressure boundaries. For low Reynolds numbers and simple geometries good agreement between these approaches was found.

Apart from the evaluation of the boundary conditions, we studied two common implementations of the lattice-Boltzmann model in 3D simulations. It was shown that within the D_3Q_{15} model, an unphysical checkerboard effect can be found, which generates spurious conservations of momentum and mass of two distinct populations of particles. For some stationary flows, this unphysical effect generates unphysical patterns in the hydrodynamic fields. The overall macroscopic behavior still seemed to be satisfactory.

Finally, we presented a new method for reducing the number of time steps that is needed to reach the steady state for body-force driven flows. In many lattice-Boltzmann simulations, the complete time evolution of the system is computed with a constant body force starting from some initial velocity and pressure fields. The number of time steps which is required to reach the steady state can then be very large for systems with a small solid fraction. By using the new Iterative Momentum Relaxation (IMR) scheme, the saturation time can be significantly reduced.

REFERENCES

1. R. Benzi, S. Succi, and M. Vergassola, The lattice-Boltzmann equation—Theory and applications, *Phys. Rep.* **3**, 145 (1992).
2. S. Chen, Z. Wang, X. Shan, and G. Doolen, Lattice-Boltzmann computational fluid dynamics in three dimensions, *J. Stat. Phys.* **68**, 379 (1992).
3. D. H. Rothman and S. Zaleski, *Lattice Gas Cellular Automata* (Cambridge Univ. Press, Cambridge, UK, 1997).
4. S. Chen and G. D. Doolen, Lattice Boltzmann method for fluid flows, *Ann. Rev. Fluid Mech.* **30**, 329 (1998).
5. D. Kandhai, A. Koponen, A. Hoekstra, M. Kataja, J. Timonen, and P. M. A. Sloot, Lattice-Boltzmann hydrodynamics on parallel systems, *Comput. Phys. Comm.* **111**, 14 (1998).
6. G. McNamara and G. Zanetti, Use of the Boltzmann equation to simulate lattice-gas automata, *Phys. Rev. Lett.* **61**, 2332 (1988).
7. F. J. Higuera and J. Jemenez, Boltzmann approach to lattice gas simulations, *Europhys. Lett.* **7**, 663 (1989).
8. F. J. Higuera, S. Succi, and R. Benzi, Lattice gas-dynamics with enhanced collisions, *Europhys. Lett.* **9**, 345 (1989).
9. Y. H. Qian, D. d'Humieres, and P. Lallemand, Lattice BGK models for Navier–Stokes equation, *Europhys. Lett.* **17**, 479 (1992).
10. A. J. C. Ladd, Numerical simulations of particulate suspensions via a discretized Boltzmann equation. Part 1. Theoretical foundation, *J. Fluid Mech.* **271**, 285 (1994); A. J. C. Ladd, Numerical simulations of

particulate suspensions via a discretized Boltzmann equation. Part 2. Numerical results, *J. Fluid Mech.* **271**, 311 (1994).

11. G. K. Batchelor, *An Introduction to Fluid Dynamics* (Cambridge Univ. Press, Cambridge, UK, 1967).
12. C. Aidun and Y. Lu, Lattice-Boltzmann simulation of solid particles suspended in fluid, *J. Stat. Phys.* **81**, 49 (1995).
13. O. Behrend, Solid-fluid boundaries in particle suspension simulations via the lattice Boltzmann method, *Phys. Rev. E* **52**, 1164 (1995).
14. D. Ziegler, Boundary conditions for lattice Boltzmann simulations, *J. Stat. Phys.* **71**, 1171 (1993).
15. P. Skordos, Initial and boundary condition for the lattice Boltzmann method, *Phys. Rev. E* **48**, 4823 (1993).
16. D. Noble, J. Georgiadis, and R. Buckius, Direct assessment of lattice Boltzmann hydrodynamics and boundary conditions for recirculating flows, *J. Stat. Phys.* **81**, 17 (1995).
17. D. Noble, S. Chen, J. Georgiadis, and R. Buckius, A consistent hydrodynamic boundary condition for the lattice Boltzmann method, *Phys. Fluids* **7**, 203 (1995).
18. D. Noble, J. Georgiadis, and R. Buckius, Comparison of accuracy and performance of lattice Boltzmann and finite difference simulations of steady viscous flow, *Int. J. Numer. Methods Fluids* **23**, 1 (1996).
19. S. Chen, D. Martinez, and R. Mei, On boundary conditions in lattice Boltzmann methods, *Phys. Fluids* **8**, 2527 (1996).
20. O. Filippova and D. Hänel, Lattice Boltzmann simulation of gas-particle flow in filters, *Comput. & Fluids* **26**, 697 (1997).
21. F. Nannelli and S. Succi, The lattice-Boltzmann equation on irregular lattices, *J. Stat. Phys.* **68**, 401 (1992).
22. N. Cao, S. Chen, S. Jin, and D. Martinez, Physical symmetry and lattice symmetry in lattice Boltzmann method, *Phys. Rev. E* **55**, 55 (1997).
23. X. He, L. S. Luo, and M. Dembo, Some progress in lattice Boltzmann method. Part 1. Non-uniform mesh grids, *J. Comput. Phys.* **129**, 357 (1996).
24. X. He, Q. Zou, L. S. Luo, and M. Dembo, Analytical solutions of simple flow and analysis of non-slip boundary conditions for the lattice Boltzmann BGK model, *J. Stat. Phys.* **87**, 115 (1996).
25. A. Koponen, D. Kandhai, E. Hellén, M. Alava, A. Hoekstra, M. Kataja, K. Niskanen, P. Sloot, and J. Timonen, Permeability of three-dimensional random fiber webs, *Phys. Rev. Lett.* **80**, 716 (1998).
26. Q. Zou and X. He, On pressure and velocity boundary conditions for the lattice Boltzmann BGK model, *Phys. Fluids* **9**, 1591 (1997).
27. R. Maier, R. Bernard, and D. Grunau, Boundary conditions for the lattice Boltzmann method, *Phys. Fluids* **8**, 1788 (1996).
28. U. Frish, B. Hasslacher, and Y. Pomeau, Lattice-gas automata for the Navier–Stokes equations, *Phys. Rev. Lett.* **56**, 1505 (1986).
29. S. Hou, Q. Zou, S. Chen, G. Doolen, and A. Cogley, Simulation of cavity flow by the lattice Boltzmann method, *J. Comput. Phys.* **118**, 329 (1995).
30. M. A. Gallivan, D. R. Noble, J. G. Georgiadis, and R. O. Buckius, An evaluation of the bounce-back boundary condition for lattice Boltzmann simulations, *Int. J. Numer. Methods Fluids* **25**, 249 (1997).
31. J. A. Kaandorp, C. Lowe, D. Frenkel, and P. M. A. Sloot, Effect of nutrient diffusion and flow on coral morphology, *Phys. Rev. Lett.* **77**, 2328 (1996).
32. D. Kandhai, D. Vidal, A. Hoekstra, H. Hoefsloot, P. Iedema, and P. M. A. Sloot, Lattice-Boltzmann and finite element simulations of fluid flow in a SMRX mixer, accepted for publication.
33. D. Koch and A. Ladd, Moderate Reynolds number flows through periodic and random arrays of aligned cylinders, *J. Fluid Mech.* **439**, 31 (1997).
34. I. Ginzbourg and P. Adler, Boundary flow condition analysis for the three-dimensional lattice Boltzmann method, *J. Phys. II France* **4**, 191 (1994).
35. T. Inamuro, M. Yoshino, and F. Ogino, A non-slip boundary condition for lattice Boltzmann simulations, *Phys. Fluids* **7**, 2928 (1995).
36. I. Ginzbourg and D. d'Humiéres, Local second-order boundary methods for lattice Boltzmann models, *J. Stat. Phys.* **84**, 927 (1996).

37. L. Wagner, Pressure in lattice Boltzmann simulations of flow around a cylinder, *Phys. Fluids* **6**, 3516 (1994).
38. L. Wagner and F. Hayot, Lattice Boltzmann simulations of flow past a cylindrical obstacle, *J. Stat. Phys.* **81**, 63 (1995).
39. B. Ferréol and D. H. Rothman, Lattice-Boltzmann simulations of flow through Fontainebleau sandstone, *Transport Porous Media* **20**, 3 (1995).
40. Y. H. Qian, S. Succi, and S. A. Orszag, Recent advances in lattice Boltzmann computing, *Annu. Rev. Comp. Phys.* **3**, 195 (1992).
41. N. S. Martys and H. Chen, Simulation of multicomponent fluids in complex three-dimensional geometries by the lattice Boltzmann method, *Phys. Rev. E* **53**, 743 (1996).
42. W. Miller, Flow in the driven cavity calculated by the lattice Boltzmann method, *Phys. Rev. E* **51**, 3659 (1995).